Appl Phys B (2009) 94: 119–125
DOI 10.1007/s00340-008-3283-0

Applied Physics B
Lasers and Optics

Imaging measurements of atomic iron concentration with laser-induced fluorescence in a nanoparticle synthesis flame reactor

C. Hecht · H. Kronemayer · T. Dreier · H. Wiggers · C. Schulz

Received: 23 June 2008 / Revised version: 17 September 2008 / Published online: 11 November 2008

Abstract The iron-atom concentration distribution as well as the gas-phase temperature was measured via laser-induced fluorescence (LIF) during iron-oxide nanoparticle synthesis in a low-pressure hydrogen/oxygen/argon flame reactor using ironpentacarbonyl ($Fe(CO)_5$) as precursor. Temperature measurements based on multi-line NO-LIF imaging are used to correct for temperature-dependent ground-state populations. The concentration measurement is calibrated based on line-of-sight absorption measurements. The influence of the precursor on the flame is observed at precursor concentrations larger than 70 ppm as the flame front moves closer to the burner surface with increasing $Fe(CO)_5$ concentration.

PACS 42.62.Fi

1 Introduction

A variety of synthesis strategies for nanoparticles from gas-phase reactions has been described in the literature [1–3]. Highly-defined conditions allow the synthesis of specific materials with narrow size distribution [4] and, for example, variable stoichiometry [5]. A promising route for the synthesis of these particles with high purity is the low-pressure flame reactor. In this reactor, the strategy to create iron-oxide nanoparticles is to pyrolytically decompose a gaseous precursor ($Fe(CO)_5$) using the heat of the flame. The created iron atoms build iron dimers and iron oxide molecules with the oxygen of the flame. Those molecules agglomerate to nanoparticles.

These particles are of interest for several industrial uses [6]. The properties of the synthesized particles can be influenced by varying the reaction conditions, like flame temperature, fuel/oxygen equivalence ratio, pressure, and precursor concentration. The final properties of the particles depend on the temporal history of the above mentioned parameters. Therefore, if the generation of particles with well-defined conditions is desired, homogeneous reaction conditions are essential. In situ measurements of concentration and temperature distribution, thus, give important input for modeling the synthesis process and for apparatus design. Laser-based techniques enable non-intrusive in situ measurements of the conditions during nanoparticle formation.

The spatially-resolved measurement of atom concentrations in nanoparticle synthesis is required to further develop and validate models that describe the precursor decomposition and the subsequent cluster and particle formation and growth [7]. These models are important for the choice of operating conditions for the specific synthesis of nanomaterials as well as for the scale-up of synthesis apparatus. The formation of FeO has been observed by other groups using laser excitation in the visible range [8]. During the formation of Fe_2O_3, however, iron atoms in different oxidation states from Fe (0) to Fe (III) occur in the flame. The fluorescence signal of iron has been widely used in medical and astronomical applications [9]. Several spectroscopic databases for iron atoms exist [10]. To our knowledge, until now LIF imaging measurements of iron atom concentration in

C. Hecht (✉) · H. Kronemayer · T. Dreier · H. Wiggers · C. Schulz
IVG, Universität Duisburg-Essen, Lotharstr. 1, 47057 Duisburg, Germany
e-mail: christian.hecht@uni-due.de
Fax: +49-203-3793087

H. Wiggers · C. Schulz
CeNIDE, Center for Nanointegration Duisburg-Essen, 47057 Duisburg, Germany

high-temperature reaction systems for nanoparticle synthesis have not been published. Previous studies used seeded indium LIF for temperature imaging in flames based on two-line excitation [11].

Metal–organic compounds are known to strongly interact with flame chemistry. Ironpentacarbonyl ($Fe(CO)_5$), that is frequently used as a precursor for iron oxide nanoparticles, is known to be a flame inhibitor [12]. Therefore, it is important to study its influence on the temperature field as a function of precursor concentration. Additionally, temperature information is required to correct Fe atom LIF measurements for temperature-dependent variations of the ground-state population.

Temperature distributions in the same low-pressure flame as reported here but in the absence of metal organic precursors have been measured by us in a previous work [13] based on multiline NO-LIF imaging. A similar strategy has been used before for measurements of the temperature along a line by Hartlieb et al. [14]. Our imaging technique has been validated and tested for different types of flames [15, 16], and yields two-dimensional temperature fields from cross-sectional LIF imaging experiments throughout the reactor. It is robust against elastic scattering and interfering signal because temperature is determined from the spectral shape of LIF excitation spectra rather than signal intensities as, e.g., in two-line LIF thermometry methods [17]. Therefore, it could be applied here with minor modifications to the excitation wavelength range also to particle-laden flames. The fundamentals of NO-LIF thermometry are described elsewhere [13, 18].

2 Experimental setup

A tunable, narrow-band KrF excimer laser (248 nm, $\Delta\nu \sim 0.3\ \mathrm{cm}^{-1}$, Lambda Physik EMG 150 TMSC) is frequency-shifted to 225 nm in a Raman cell filled with 6 bar hydrogen to its first anti-Stokes line, enabling excitation of specific atomic Fe transitions in the a^5D–$^5F^0$ and NO in the A-X (0, 0) band. The laser beam is expanded in the horizontal direction and compressed in the vertical direction with two cylindrical lenses $f = 1000$ mm and 300 mm, respectively, to form a light sheet of approximately $50 \times 10\ \mathrm{mm}^2$. This comparably large beam cross-section was chosen to prevent saturation of NO transitions during temperature measurements. Previous measurements showed an onset of saturation that influences temperature measurements at laser fluences of $\sim$10 kW/cm^2 [13]. The geometry of the present experiment does not require high spatial resolution in the direction normal to the light sheet; therefore, a large cross-section light sheet could be applied to reduce laser fluence. The LIF signal is recorded with an intensified CCD camera (LaVision) at 90° relative to the laser direction.

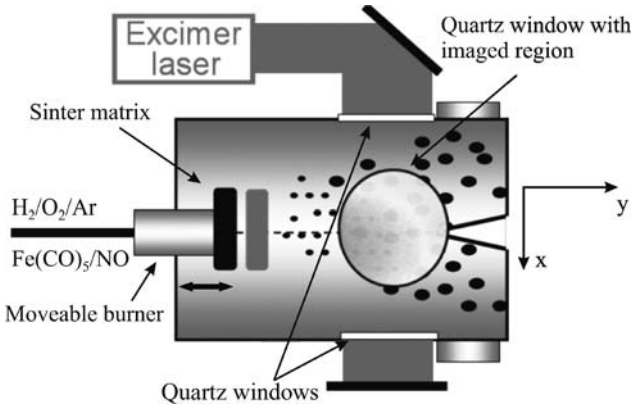

Fig. 1 Horizontal cut through the flat-flame reactor. Optical access is provided by fused silica windows on three sides of the combustion chamber. The burner head can be moved horizontally relative to the windows and the sampling nozzle

Elastically-scattered light is suppressed by four long-pass filters (230 nm, LayerTec). The same setup has been used before for NO thermometry in low-pressure flames [13]. For measurements of emission spectra, an imaging spectrograph (ARC, $f = 155$ mm, $f_\# = 4\,300$ lines/mm grating) was used.

The reaction chamber is 300 mm long and has a diameter of 150 mm. A hydrogen/oxygen/argon flame is stabilized on a water-cooled sintered stainless-steel matrix of 36 mm in diameter. It can be moved horizontally within the chamber to vary the distance from 0–190 mm to a skimmer nozzle that is used for extraction of particle-laden gas for molecular-beam mass spectrometric analysis [4]. Optical access is possible through fused silica windows with a diameter of 50 mm at both sides and on the top of the reaction chamber (see Fig. 1). The flow rates used for the synthesis of Fe_2O_3 nanoparticles were 770 sccm H_2 and 1040 sccm O_2 resulting in an equivalence ratio of this lean mixture is $\phi = 0.37$. The flow of argon (that carried between 140 and 850 ppm $Fe(CO)_5$) varied slightly for the different flames and was 575, 545, and 470 sccm for the flames with 35, 70, and 170 ppm $Fe(CO)_5$, respectively. During the measurements, the chamber pressure was set to 3 kPa. The flow velocity inside the reactor reaches a few m/s. An overview of the burner is given in Fig. 1. Further details on the reactor are given in [19].

In order to observe the entire reaction zone the burner head was moved to different positions relative to the observation area (defined by the window position). The data of the individually observed sections ($50 \times 30\ \mathrm{mm}^2$) were plotted next to each other to visualize results for the entire accessible zone ($50 \times 90\ \mathrm{mm}^2$) inside the reaction chamber. It should be noted, however, that the flame slightly changes when moving the burner head relative to the chamber.

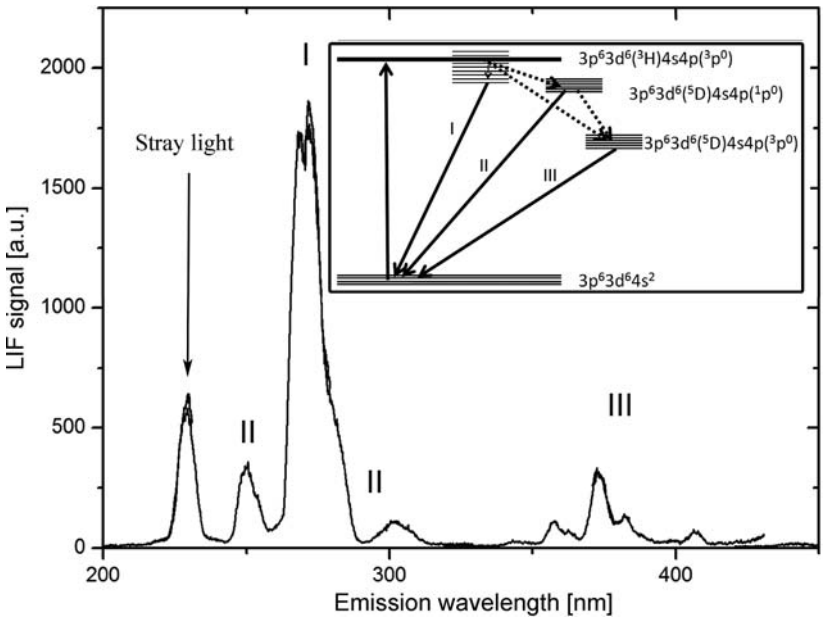

Fig. 2 LIF emission spectrum of iron excited at 44415 cm^{-1}. The relevant energy levels are given in the insert

3 Results

3.1 Fe-LIF spectroscopy

For Fe-LIF detection, two excitation wavelengths of iron were chosen within the fundamental (248 nm) and the Raman-shifted (225 nm) tuning range of the KrF excimer laser. At 225 nm a weak transition from the ground state ($3p^63d^64S^2$) to an excited state ($3p^63d^6(a^3F)4s4p(^3P^0)$) is used [10]. Due to its weak transition probability, the laser is not significantly attenuated inside the reactor for the present experimental conditions. Figure 2 shows the spectrally-resolved fluorescence after excitation at 44415 cm^{-1}. In addition the origin of the depicted fluorescence bands is given in the relevant Fe energy level diagram shown in the inset. Direct emissions from the $3p^63d^6(a^3F)4s4p(^3P^0)$ system is present at 268 nm (I). Additionally, an emission band (II) upon 248 nm excitation is observed. This is due to inter-system crossing to the $3p^63d^6(^5D)4s4p(^1P^0)$ system. Despite the fact that the transition probability for the emission process is higher in the latter case by a factor of 200, the observed signal is weaker because of the underlying spin-forbidden inter system crossing. Additional weak emissions from lower lying states populated by further ISC can be observed around 300 nm (III).

The mentioned second transition at 248 nm (40257 cm^{-1}) also originates from the ground state, but reaches a different excited state ($3p^63d^6(^5D)4S4P(^1P^0)$, not shown in Fig. 3). This transition is the strongest of all iron transitions in this spectral window. Hence, at the relevant Fe concentration levels the laser beam is nearly completely absorbed within the first 10 to 20 mm inside the reactor.

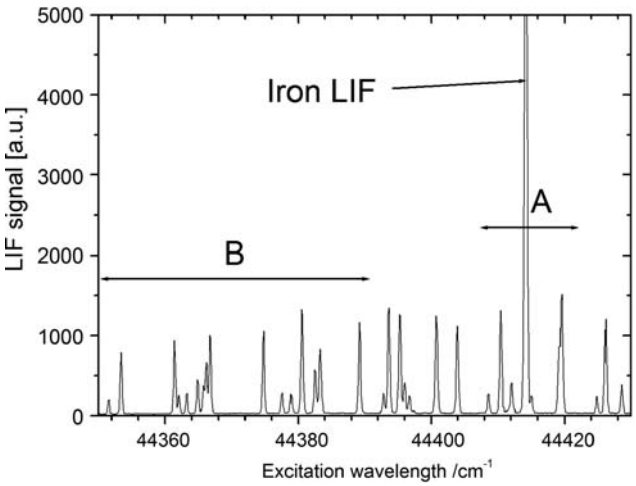

Fig. 3 Fluorescence excitation spectrum from within the nanoparticle reactor. NO-LIF and Fe-LIF signal is visible. The spectral range that was previously used for NO thermometry [13] marked "A" and the adjusted scan range for systems with Fe ("B") are indicated

3.2 Temperature measurement via NO multi-line thermometry

For correction for temperature effects on the Fe-LIF diagnostics the temperature profile inside the reactor was measured. For these measurements, 200 ppm of NO was seeded into the flame. This concentration is low enough to not influence the flame chemistry. Temperature imaging measurements were done with multi-line NO-LIF thermometry [20]. LIFSim [21] was used to evaluate the NO-LIF excitation spectra.

The temperature profiles were taken, using NO transitions within the excitation range of 44350–44390 cm^{-1}.

This spectral range is different from the one previously used [13]. It was chosen to avoid interference from iron LIF at 44415 cm^{-1}, with the Fe-LIF signal one order of magnitude stronger than NO LIF. Figure 3 shows the LIF excitation spectra in a flame doped with 200 ppm NO and 70 ppm $Fe(CO)_5$ with detection at the center of the flame, 40 mm away from the burner head. The previously used (A) and the new scan range (B) for NO-LIF multi-line thermometry is shown. In order to maintain the temperature accuracy, the excitation wavelength range was doubled compared to that in [13] which also doubles the measurement time to ∼30 min per measurement. For Fe(I)-LIF detection, the strong transition at 44415 cm^{-1} ($3p^6 3d^6 4S^2$ to $3p^6 3d^6(a^3F)4S4P(^3P^0)$) was used for measuring the iron-atom distribution [10].

3.3 Temperature dependence of Fe LIF

The 225 nm and the 248 nm transitions used in this investigation originate from the same electronic ground state. Its temperature-dependent population was evaluated to allow for quantitative measurements also in systems with inhomogeneous temperature distribution. The partition function of iron atoms was calculated, using the five states from the NIST database [10] with the lowest energy. Higher energetic states have an energy level too high to be populated. With this partition function, the fractional population of the ground state at temperature T was calculated.

3.4 Quantification of Fe LIF

In order to estimate the effect of the fluorescence quenching on the species measurements, we carried out a preliminary investigation of the lifetimes of the observed emissions. The lifetime was measured with ns laser pulse excitation and detection with an ICCD camera with a detection gate of ∼5 ns and a variable delay relative to the laser pulse. Fluorescence lifetimes were obtained by single exponential fits to the data.

Figure 4 shows the fluorescence intensity decay of transition (I) emitting at 268 nm for two different temperatures, i.e., locations in the flame. This emission band was selected because its upper level exhibits the same electronic configuration (angular momentum quantum number) as the excited ground state level which allows calculating the decay rate for the spin-allowed transition. Without quenching the natural lifetime of this transition is known to be around 52 ns [10]. Our measurements yield lifetimes of 6.4 ns for 1200 K and of 7.5 ns for 800 K with an uncertainty of 3 ns. Even though the uncertainty in these measurements is quite high it is known that quenching rates change little at higher temperatures. Therefore, the influence of the resulting error on the retrieved line intensities can be neglected when evaluating relative Fe-concentration profiles (see below).

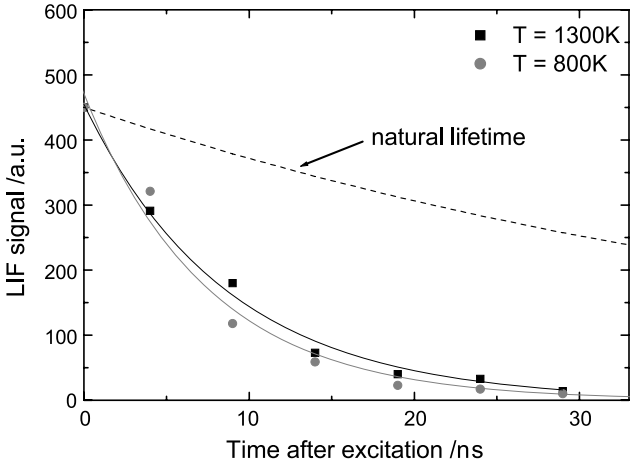

Fig. 4 Fe-LIF lifetime measurements at two different temperatures at 30 mbar in the burned gases of the $H_2/O_2/Ar$ flame. The decay according to the (known) natural lifetime is indicated by the *dashed line*

Calibration of Fe-LIF signal intensities I_λ for excitation at wavelength λ with respect to concentration is based on the measured attenuation of the laser radiation at 248 nm during passage through the flame gases [22]. Because Fe concentration and temperature vary in the observed region simultaneously, imaging measurements with 248 nm excitation were related to measurements at 225 nm excitation where the laser attenuation was negligible. The underlying procedure that evaluates local laser attenuation and then derives local concentration is described in the following paragraph.

The intensity of the fluorescence light $I_\lambda(x)$ at location x is proportional to the local laser intensity $I^\lambda_{\mathrm{Laser}}(x)$, the local concentration of the absorbing atoms $c^*(x)$ (which depends on the total local iron atom concentration $c(x)$ corrected for temperature using the Boltzmann factor $c^*(x) = c(x)f(T(x))$) and a fluorescence yield factor k_λ that depends on the excitation wavelength λ. The local signal intensity $I_\lambda(x)$ for both excitation wavelengths is thus

$$I_{225}(x) = k_{225} \cdot c^*(x) \cdot I^{225}_{\mathrm{Laser}}(x), \quad (1)$$

$$I_{248}(x) = k_{248} \cdot c^*(x) \cdot I^{248}_{\mathrm{Laser}}(x). \quad (2)$$

The LIF-signal intensity distribution for both excitation wavelengths was recorded along the laser propagation axis (x-axis in Fig. 1) and profiles 20 mm in length were extracted for each excitation wavelength under identical reaction conditions. The ratio of both signals $R(x)$ is determined. If negligible self absorption of fluorescence radiation is assumed in the detection beam path, local concentration cancels and because both excitation schemes excite Fe from the same ground state level, the Boltzmann factor cancels as well. Because the laser intensity at 225 nm is not attenuated

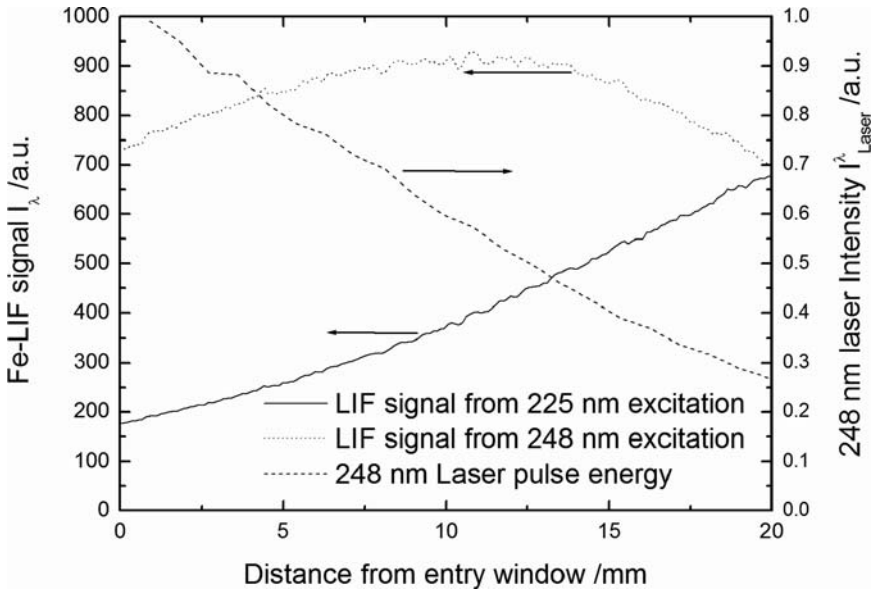

Fig. 5 Comparison of the observed Fe-LIF signal after excitation at 225 and 248 nm, respectively. From the ratio of both signals the local variation in 248 nm laser intensity is derived according to (3) assuming negligible laser attenuation at 225 nm

the ratio $R(x)$ of both LIF signal profiles is then proportional to the local laser intensity $I^{248}_{\mathrm{Laser}}(x)$ only (cf. Fig. 5)

$$R(x) = \frac{I_{248}(x)}{I_{225}(x)} = \frac{k_{248}}{k_{225}} \cdot I^{248}_{\mathrm{Laser}}(x). \tag{3}$$

The local variation in laser intensity was then evaluated in spatial increments of $\Delta x = 1$ mm. From the comparison of the laser intensity at location $x(I^0_{\mathrm{Laser}})$ and at location $(x - \Delta x)(I_{\mathrm{Laser}})$ the local absorber concentration was determined using the Beer–Lambert law (with absorption cross section σ and length l):

$$I_{\mathrm{Laser}} = I^0_{\mathrm{Laser}} \cdot \exp\bigl(-c^*(x) \cdot l \cdot \sigma\bigr), \tag{4}$$

$$\frac{R(x)}{R(x - \Delta x)} = \exp\bigl(-c^*(x) \cdot \Delta x \cdot \sigma_{248}\bigr), \tag{5}$$

$$c^*(x) = \frac{1}{\Delta x \cdot \sigma_{248}} \ln\left(\frac{R(x - \Delta x)}{R(x)}\right). \tag{6}$$

To arrive at the true concentration values, the Boltzmann factor was calculated for each point using the temperature data from NO-LIF thermometry. This calculated concentration was compared with the measured 225 nm LIF signal intensity (Fig. 6) to obtain a conversion factor. From repeated measurements a standard error of 20% was evaluated for this method.

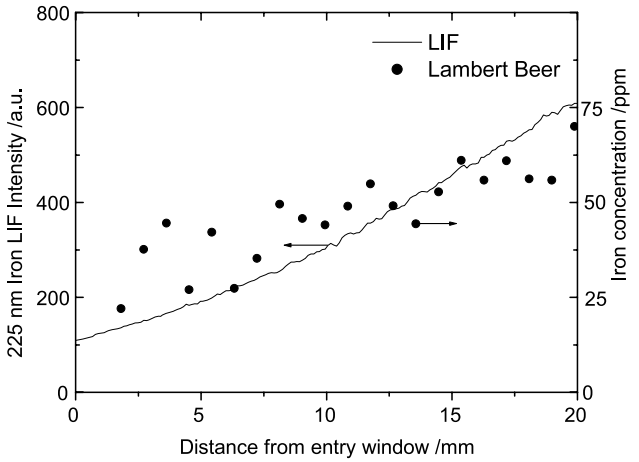

Fig. 6 Comparison of measured iron LIF intensity excited at 225 nm (*solid line*) and concentration of iron calculated from the absorption measurements at 248 nm (*solid symbols*)

4 Discussion

Figure 7(a) shows measured two-dimensional temperature and Fe(I)-concentration distributions for a flame with 70 ppm $Fe(CO)_5$. One-dimensional profiles along the flow coordinate (y-axis in Fig. 1) were taken by averaging the temperature data for each y position within the central 10 mm of the burner chamber (between horizontal white lines in Fig. 7(a)). Figure 7(b) shows the resulting Fe(I)-concentration profiles for three different $Fe(CO)_5$ concentrations. As described in Sect. 2, the different zones of the flame were investigated by translating the burner to different positions within the chamber which slightly changes the flame conditions. Therefore, the graphs show steps at the limits of the individual measurement sections.

Temperature profiles for the same conditions are shown in Fig. 7(c). It can be observed that the formation of iron atoms starts earlier (i.e., closer to the burner surface) when higher initial concentrations of $Fe(CO)_5$ are seeded into the fresh gases. Higher $Fe(CO)_5$ initial concentrations are also associated with a faster rise of the temperature profile and

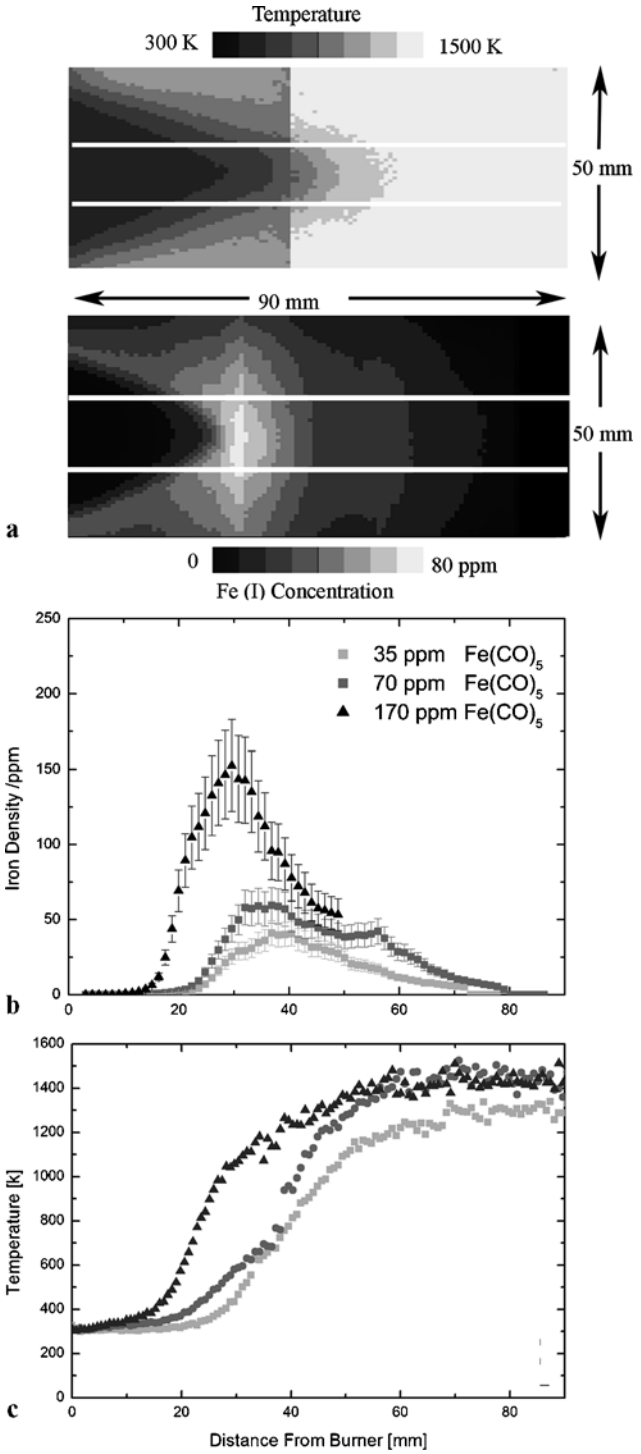

Fig. 7 (**a**) Temperature and iron (Fe(I)) concentration distribution with 70 ppm of $Fe(CO)_5$ in the fresh gases for three positions of the burner within the reactor chamber (see text). (**b**) Iron-atom density averaged in the central 10 mm along the *y* axis (marked in (**a**)) for three $Fe(CO)_5$ concentrations in the fresh gases; (**c**) Temperature profiles for the same region marked in (**a**)). Discontinuities in the images and profiles result from the combination of measurements with different burner positions (see text)

higher end gas temperatures, i.e., the flame front moves closer to the burner surface.

For all seeding levels investigated iron atom formation starts at temperatures around 380–420 K. In the kinetic scheme suggested in [12], the dissociation of $Fe(CO)_5$ to $Fe(CO)_4 + CO$ is considered the rate-determining step. Fast consecutive reactions then lead to the formation of iron atoms. Accordingly, in the experiments, as soon as iron is detected, dissociation of $Fe(CO)_5$ has started. The iron concentration reaches its maximum approximately 15 mm downstream of the point where its generation started. Further downstream the formation of clusters, iron oxide and other oxidation states of Fe strongly reduces the measured Fe(I) concentration. For iron atom consumption in non-oxidizing systems the reaction $2Fe \rightarrow Fe_2$ was determined as the rate-determining step [7].

With 35 ppm $Fe(CO)_5$ in the fresh gases the maximum concentration of iron atoms inside the flame is also around 30 ppm. With higher precursor concentration, the highest attained iron concentration is less than the equivalent concentration of $Fe(CO)_5$, and the zone in which iron atoms can be found is expanded.

5 Conclusions

For the validation of numerical simulations of the growth of flame-generated nanoparticles, species distribution and temperature inside the reactor must be known. $Fe(CO)_5$ was added to the flame, as a precursor for iron-oxide nanoparticle generation. Iron (I) atoms formed during the dissociation of $Fe(CO)_5$ were visualized with laser-induced fluorescence imaging inside the reaction zone. The temperature was measured in the same region via multi-line NO-LIF thermometry. With increasing $Fe(CO)_5$ concentration the flame front was found to move closer to the burner and the temperature profile changes significantly. For absolute concentration measurements, the LIF signal intensities were corrected for temperature effects and calibrated using an absorption-based LIF strategy.

Acknowledgement Funding by the German Research Foundation (DFG) within SFB 445 is gratefully acknowledged.

References

1. S.E. Pratsinis, Prog. Energy Combust. Sci. **24**, 197 (1998)
2. G. Buxbaum, G. Pfaff, *Industrial Inorganic Pigments* (Wiley-VCH, Weinheim, 2005)
3. C. Granquist, L. Kish, W. Marlow, *Gas-Phase Nanoparticle Synthesis* (Springer, Heidelberg, 2004)
4. P. Roth, Proc. Combust. Inst. **31**, 1773 (2007)
5. P. Ifeacho, T. Huelser, H. Wiggers, C. Schulz, P. Roth, Proc. Combust. Inst. **31**, 1805 (2007)

6. G.E. Fougere, J.R. Weertman, Nanostruct. Mater. **5**, 127 (1995)
7. A. Giesen, A. Kowalik, P. Roth, Phase Transit. **77**, 115 (2004)
8. B.K. McMillin, P. Biswas, M.R. Zachariah, J. Mater. Res. **11**, 1552 (1996)
9. H. Kunieda, T.J. Turner, A. Hisamitsu, K. Koyama, R. Mushotzky, Y. Tsusaka, Nature **345**, 786 (1990)
10. Y. Ralchenko, NIST Atomic spectra Darabase (Version 3.1.2) [Online]. Available: http://physics.nist.gov/asd3 [2007, August 1]. National Institute of Standards and Technology (2007)
11. I.S. Burns, J. Hult, C.F. Kaminski, Appl. Phys. B **79**, 491 (2004)
12. M.D. Ruminger, Combust. Flame **116**, 207 (1999)
13. H. Kronemayer, P. Ifeacho, C. Hecht, T. Dreier, H. Wiggers, C. Schulz, Appl. Phys. B **88**, 373 (2007)
14. A.T. Hartlieb, B. Atakan, K. Kohse-Höinghaus, Appl. Phys. B **70**, 435 (2000)
15. T. Lee, W.G. Bessler, H. Kronemayer, C. Schulz, J.B. Jeffries, R.K. Hanson, Appl. Opt. **44**, 6718 (2005)
16. H. Kronemayer, W.G. Bessler, C. Schulz, Appl. Phys. B **81**, 1071 (2005)
17. M. Tamura, J. Luque, J.E. Harrington, P.A. Berg, G.P. Smith, J.B. Jeffries, D.R. Crosley, Appl. Phys. B **66**, 503 (1998)
18. W.G. Bessler, C. Schulz, Appl. Phys. B **78**, 519 (2004)
19. D. Lindackers, M.G.D. Strecker, P. Roth, C. Janzen, S.E. Pratsinis, Combust. Sci. Technol. **123**, 287 (1997)
20. W.G. Bessler, C. Schulz, Appl. Phys. B **78**, 519 (2004)
21. W.G. Bessler, C. Schulz, V. Sick, J.W. Daily, A versatile modeling tool for nitric oxide LIF spectra (www.lifsim.com) (3rd Joint meeting of the US sections of The Combustion Institute, Chicago, 2003, PI05)
22. M.J. Dyer, D.R. Crosley, Opt. Lett. **7**, 382 (1982)